Stress-Induced Shift of Band Gap in ZnO Nanowires from Finite-Element Modeling

Lukasz Kuna* and John Mangeri
Department of Physics, University of Connecticut, Storrs, Connecticut 06269, USA

Pu-Xian Gao
Department of Materials Science and Engineering and Institute of Material Science, University of Connecticut, Storrs, Connecticut 06269, USA

Serge Nakhmanson†
Department of Materials Science and Engineering and Institute of Material Science, University of Connecticut, Storrs, Connecticut 06269, USA and Department of Physics, University of Connecticut, Storrs, Connecticut 06269, USA

(Received 28 March 2017; revised manuscript received 10 July 2017; published 27 September 2017)

Attractive mechanical, optical, and electronic properties of semiconducting ZnO nanowires make them prime candidates for a variety on energy-harvesting technologies, including photovoltaics and piezoelectric nanogenerators. In order to enhance the efficiency and versatility of such devices, it is paramount to elucidate the connections between the different property realms, i.e., to establish how mechanical distortions can affect the electronic and optical response of the nanowires, depending on their size, shape, and morphology. For example, it was recently demonstrated that band-gap downshifts of up to −0.1 eV can be induced in monolithic ZnO nanowires by an application of tensile strain [see Wei *et al.*, Nano Lett. **12**, 4595 (2012)]. Here, we conduct mesoscale-level, finite-element-method-based modeling of the coupled elastic and electronic properties of both already-synthesized monolithic ZnO nanowires and yet-to-be-fabricated Zn-ZnO core-shell structures with diameters ranging from 100 to 800 nm. Our investigation suggests that, after an optimization of the size, shape, and mutual crystallographic orientations of the core and shell regions, core-shell nanowires can exhibit downward band-gap shifts of up to −0.3 eV (i.e., approximately 10% of the stress-free ZnO band-gap value) under tensile distortions, which can greatly expand the utility of such nanostructures for optoelectronic applications.

DOI: 10.1103/PhysRevApplied.8.034031

I. INTRODUCTION

Semiconducting ZnO (with its direct band gap $E_g = 3.37$ eV [1]) is one of the very few *dominant* materials for nanoscale technologies, by virtue of its low cost, negligible environmental impact, and the wide variety of possible nanostructures that can be conveniently fabricated from it [2–6]. Such zero- and one-dimensional (1D) geometries as nanobelts [2,4,7], nanorods and nanowires [4,8,9], and nanorings and nanohelixes [2,4] have been made from ZnO and integrated with other microscopic and nanoscopic building blocks [10,11], including core-shell arrangements [12]. Prospective applications of these nanostructures as device components range from field-effect transistors [13,14] and power generators for wearable and biomedical electronics [15], including nanorobots [4,16], to photodetectors and photovoltaics [16–23], as well as mechanical [24] and chemical sensors [18,25].

Among all of the aforementioned nanoscale configurations, ZnO nanowires and nanorods stand apart as particularly versatile structures for employment in energy-harvesting applications, such as photovoltaics [22,23,26–30], photocatalysis [31,32], and piezoelectric nanogenerators [4]. Although *static* modulation of the wire electronic properties has been accomplished—e.g., by means of chemical doping [33,34]—their *dynamical* tuning may be required for future generations of energy-harvesting devices. For example, large-band-gap down-shifts may need to be produced (presumably by a combination of different mechanisms for ZnO, which is a wide-band-gap semiconductor) to utilize a wider range of the solar spectrum for more efficient photovoltaic energy conversion. A number of very recent experimental and theoretical efforts have focused on investigating the possibilities of dynamical band-gap modulation by elastic distortions of ZnO nanowires [35–38]. In particular, Wei *et al.* measured band-gap changes induced by axial stretching of wires 100 to 800 nm in diameter, reporting a maximum gap change of 100 meV in a 100-nm wire subject to 7.8% tension [35].

While the results of these initial studies are encouraging, the effects of nanowire *shape*, *size*, and *morphology*—all paramount for the design of more efficient nano-electromechanical devices—on the strength of band-gap tuning have not been explored. Here, we utilize a

*lukasz.kuna@uconn.edu
†serge.nakhmanson@uconn.edu

finite-element-method (FEM)-based computational approach [39] with material parameters obtained from both experimental data and *ab initio* simulations to evaluate the mechanical and electronic properties of model systems corresponding to the actual nanowires characterized by Wei *et al.* [35], obtaining excellent agreement with the experimental results. Furthermore, we attempt to optimize the influence of the geometrical and microstructural factors on the band-gap modulation by designing Zn-ZnO core-shell nanowire systems that, compared to their *monolithic* counterparts, should display much larger band-gap down-shifts under similar levels of elastic distortions.

The rest of this paper is organized as follows. In Sec. II, we introduce our working approach, discussing construction of geometrical models of nanowires, parametrization of elastic and electronic properties, and the involved computational methodology. In Sec. III, we present the results of our calculations, focusing initially on models of monolithic nanowires, equivalent to those studied by Wei *et al.* [35], then on yet-to-be-synthesized Zn-ZnO core-shell systems. In both cases, the influence of model shape, size, and microstructure on its behavior is thoroughly discussed. Finally, in Sec. IV, we conclude, emphasizing a few ideas that may be particularly fruitful for achieving the strongest strain-induced band-gap modulation in such systems.

II. METHODS

A. Structural models

Structural nanowire models utilized in the FEM computations within this investigation are created and meshed using TRELIS [40]. An unstructured grid of tetrahedrons (TetMesh) is employed for the meshing of all of the models. The finite-element mesh spacing is chosen to ensure sufficient resolution and convergence of the elastic fields within and at the surfaces of each structural block, including (thin) shells and core-to-shell interfaces in the core-shell nanowire models. Simple cylindrical and hexagonal shapes, such as those displayed in Figs. 1(a) and 1(b), respectively, are used to model monolithic monocrystalline *w*-ZnO nanowires. For all of these models, the hexagonal crystallographic orientation in *w*-ZnO is aligned with the axis of the wire. The characteristic cross-section size d of the wires [the diameter in the case of a cylindrical shape, and the corner-to-corner distance in the case of a hexagonal shape, as depicted in Fig. 1(b)] is chosen to be 100, 260, and 760 nm, i.e., corresponding to the sizes studied by Wei *et al.* [35], although a variety of structures with intermediate d's are evaluated as well. Most of the studied nanowires, both monolithic and core shell, are 400 to 500 nm in length, as further length increases do not result in appreciable changes in the reported properties.

It is noteworthy that the work of Wei *et al.* does not report on any particular structural features of the wires, such as their cross-section shape, mono- or polycrystallinity, or the possible crystallographic orientation of ZnO with respect to the wire axis. Therefore, reasonable guesses for the wire microstructure have to be adopted in this investigation, as we discuss in detail below. The rationale for selecting a hexagonal shape stems from experimental evidence that many "naturally grown" ceramic wires adopt that form because of the sixfold symmetry of *w*-ZnO [41–44], or various III-V compounds, such as GaAs or GaN [45–48].

The core-shell structures studied here are displayed in Figs. 1(c), 1(d), and 1(e), and also utilize the same basic cylindrical and hexagonal shapes as the monolithic wires.

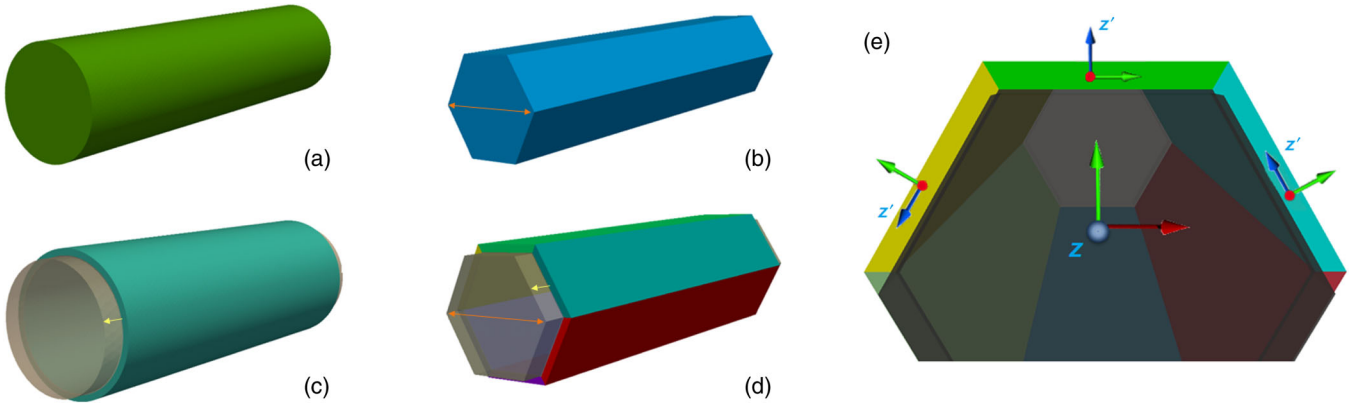

FIG. 1. Sketches of (a) monolithic cylindrical and (b) hexagonal ZnO nanowire models, as well as core-shell (c) cylindrical and (d) hexagonal Zn-ZnO nanowire models. Characteristic corner-to-corner core dimensions in hexagonal wires are indicated in (b) and (d), while core protrusions in core-shell geometries are shown by arrows in (c) and (d). In both types of core-shell models, the orientation of the hexagonal symmetry axis of Zn within the core block is aligned with the axis of the nanowire (coordinate system $\boldsymbol{x},\boldsymbol{y},\boldsymbol{z}$), while tensorial axis orientations (coordinate systems $\boldsymbol{x}',\boldsymbol{y}',\boldsymbol{z}'$) within the single (cylindrical-model) or multiple (hexagonal-model) ZnO shell blocks can be chosen individually. An example of different shell coordinate system orientations for a hexagonal core-shell system is shown in (e). Here, the global $\boldsymbol{z}$ axis is pointing away from the viewer. For clarity, $\boldsymbol{x},\boldsymbol{y}$ and $\boldsymbol{x}',\boldsymbol{y}'$ axis assignments are omitted.

In addition to the "core-diameter" and "shell-thickness" parameters (each of these can be controlled separately), the core-shell models are also characterized by "core protrusion," i.e., the distance by which the core extends beyond the shell belt, as shown in Figs. 1(c) and 1(d). As discussed in Sec. III B, this parameter has a strong influence on the nanowire behavior.

In the nanowire models, we introduce two kinds of coordinate systems. The global $\boldsymbol{x},\boldsymbol{y},\boldsymbol{z}$ system is tied to the geometrical shape of the wire, with the $\boldsymbol{z}$ direction serving as its cylindrical or hexagonal axis. The local $\boldsymbol{x}',\boldsymbol{y}',\boldsymbol{z}'$ system is tied to the orientations of the elastic-tensor axes within each material block in the model, which may be a single ZnO block in the monolithic case or multiple blocks in the core-shell case. In turn, the directions of the primed axes within each block are related to the crystallographic orientations of the specific material filling that block. Even in the case of monolithic w-ZnO wires, where the whole system is represented by a single material block, the orientations of the global and local coordinate systems do not have to coincide, which means that the elastic-tensor or crystallographic axes of ZnO may be, in principle, arbitrarily rotated with respect to the location of the global axes. However, the appreciable band-gap tunings in such systems are obtained for the case of the z' axis (i.e., the hexagonal crystallographic axis in w-ZnO), being aligned with the z axis of the nanowire; therefore, only these cases are discussed below.

For all of the core-shell systems considered here, metallic Zn (space group $P6_3/mmc$) is chosen as the core material since the Zn-ZnO combination has been already utilized for the synthesis of a variety of different core-shell structures [42,49–53]. Within the core block, the hexagonal crystallographic orientation of Zn is aligned with the axis of the wire, while the elastic-tensor or crystallographic axis orientations within single (cylindrical-geometry) or multiple (hexagonal-geometry) shell blocks are adjusted independently by the $\mathbf{Z}_1(\theta)\mathbf{X}_2(\phi)\mathbf{Z}_3(\Psi)$ sequence of Euler rotations. As in the case of the monolithic wires, the z' axis in each ZnO block is chosen to be the hexagonal crystallographic axis of w-ZnO. A sketch of possible $\boldsymbol{x}',\boldsymbol{y}',\boldsymbol{z}'$ tensor axis orientations in separate shell plates in the hexagonal core-shell configuration with a global coordinate system $\boldsymbol{x},\boldsymbol{y},\boldsymbol{z}$ is presented in Fig. 1(e). In most calculations for the hexagonal core-shell systems presented below, the orientations of the local $\boldsymbol{z}'$ axes are taken to be parallel to the global axis $\boldsymbol{z}$. Different orientations of the local $\boldsymbol{x}',\boldsymbol{y}'$ axes with respect to the plate surfaces are examined but found not to affect the results substantially (see the bottom of Sec. III for details). Material parameters in each geometric block are considered to be homogeneous, and a coherent elastic interface between the materials is assumed for each internal surface.

B. Bulk elastic properties parametrization

Within the linear elasticity approximation, the elastic energy of each nanowire model, treated as a spatial domain of volume Ω enclosed by a surface S, can be computed by utilizing the following expression:

$$U^{\varepsilon} = \int_{\Omega} \sigma_{ij}\varepsilon_{ij}dV = \frac{1}{2}\int_{\Omega} C_{ijkl}\varepsilon_{kl}\varepsilon_{ij}dV = \frac{1}{8}\int_{\Omega} C_{ijkl}\left[\frac{\partial u_k}{\partial x_l}+\frac{\partial u_l}{\partial x_k}\right]\left[\frac{\partial u_i}{\partial x_j}+\frac{\partial u_j}{\partial x_i}\right]dV. \quad (1)$$

Here, σ_{ij}, ε_{kl}, and C_{ijkl} are elastic stress, strain, and stiffness tensors, respectively, and $u_k(\mathbf{r})$ represents vector components of the displacement field with Cartesian components represented by indices $i, j, k, l = x, y, z$; summation over repeating indices is implied. In addition, a stress divergence equation,

$$\frac{\partial \sigma_{ij}}{\partial x_j} = \frac{\partial}{\partial x_j}(C_{ijkl}\varepsilon_{kl}) = \frac{\partial}{\partial x_j}\left(C_{ijkl}\frac{\partial u_k}{\partial x_l}\right) = f_i, \quad (2)$$

has to be solved concurrently with Eq. (1) for a fixed finite displacement applied at the two opposite nanowire faces, or nanowire core faces for core-shell structures, with $\pm z$ surface normals. This boundary condition is equivalent to introducing an axial elastic strain in the nanowire, with f_i being the components of the body force resulting from the distortion of the wire shape.

The bulk values of the individual components of the C_{ijkl} tensor for the involved materials, i.e., metallic Zn and w-ZnO, were obtained from the literature and are assembled in Table I. For Zn, $C_{33} \simeq C_{11}/3$, which makes the elastic properties of this structure highly anisotropic. On the other hand, although w-ZnO formally has hexagonal symmetry (space group $P6_3mc$), it is nearly elastically isotropic. In Voigt notation, its elastic stiffness coefficients are such that $C_{11} \simeq C_{33}$, $C_{12} \simeq C_{13}$ and $C_{44} \simeq C_{66} \simeq (C_{11}-C_{12})/2$. Averaged values of these coefficients can be related to the Poisson ratio ν and the Young's modulus Y—i.e., the quantities that are usually reported by experimental investigations of mechanical response in ZnO nanostructures—with the help of the Lamé parameters λ and μ [54]:

$$C_{11} = \lambda + 2\mu,$$
$$C_{12} = \lambda = \frac{\nu Y}{(1+\nu)(1-2\nu)},$$
$$C_{44} = \mu = \frac{Y}{2(1+\nu)}. \quad (3)$$

While surface elasticity [57,58] could alter the properties of some ZnO nanostructures [39,59], we find its influence to be negligible for the (relatively large) nanowire sizes

TABLE I. Bulk elastic stiffness-tensor components for metallic Zn and *w*-ZnO in reduced Voigt notation [54] in units of GPa. Averaged components for an isotropic case [54] with $C_{11} = C_{33} = 2\mu + \lambda$, $C_{12} = C_{13} = \lambda$, and $C_{44} = C_{66} = \mu$ are also given for ZnO.

	Reference	Crystal structure	C_{11}	C_{12}	C_{13}	C_{33}	C_{44}	C_{66}
Zn	[55]	hcp ($P6_3/mmc$)	163.0	30.6	48.1	60.3	39.4	65.9
ZnO	[56]	Wurtzite ($P6_3mc$)	209.7	121.1	105.1	210.9	42.5	44.3
ZnO		Isotropic	205.9	118.5			43.7	

investigated in this work. The treatment of surface elasticity within our computational approach is implemented in the same manner as in Ref. [39].

The numerical solution of Eqs. (1) and (2) on the domain Ω to obtain the equilibrium displacement field $u_k(\mathbf{r})$ and the corresponding elastic strain- and stress-tensor components $\varepsilon_{ij}(\mathbf{r})$ and $\sigma_{kl}(\mathbf{r})$ is carried out with the FERRET [60] code that is being developed by the authors within the MOOSE [61,62] multiphysics simulation framework. In all calculations, the relative residual norm is converged to less than 10^{-8}, irrespective of the applied boundary conditions or any specific variations of the model geometry within the domain Ω, such as the utilization of cylindrical or hexagonal wire shapes, or the alteration of the core-shell volume ratio.

C. Nanowire stiffening effects

Variations of elastic properties of *w*-ZnO nanowires as their size, d, diminishes have been thoroughly investigated [8,35,63–68]. There is a general agreement that nanowires start to stiffen when d becomes smaller than $d_c \sim 300$ nm; however, one group of studies reported that such changes are not significant until the diameter is less than 10–70 nm [64,65,67], while the other group finds substantial stiffening effects at diameters right below d_c [8,35,63,66].

To account for the size-dependent increase in the averaged elastic stiffness coefficients in monolithic wires with $d \leq d_c$, we use Eq. (3) to adjust the bulk parameters of Table I, utilizing the Y and ν values reported by Wang *et al.* [68] and Asthana *et al.* [8]. The modified elastic stiffness coefficients for the 100- and 260-nm wires are displayed in Table II, while, for the large-diameter 760-nm wire, the original bulk parameters are used. For representing any size-dependent stiffening effects in the core-shell structures, data obtained for *w*-ZnO thin films—rather than monolithic nanowires—would be more appropriate. However, we were not able to find any relevant data on film thickness dependence of Y and ν, and therefore the bulk elastic stiffness-tensor coefficients presented in Table I are used to model the behavior of *w*-ZnO shells.

D. Coupling the band gap to elastic distortions

Once the mechanical equilibrium is established and the corresponding displacement field is obtained, the resulting strains can then be utilized to find the position-dependent modulated ZnO band-gap energy distribution through the expression

$$E_g^{\varepsilon}(\mathbf{r}) = E_g^0 + \delta E_g(\mathbf{r}) = E_g^0 + D_1\varepsilon_{z'z'}(\mathbf{r}) + D_2[\varepsilon_{x'x'}(\mathbf{r}) + \varepsilon_{y'y'}(\mathbf{r})]. \quad (4)$$

This formula is a linear approximation for the $\mathbf{k}\cdot\mathbf{p}$ deformation-potential model for the strain-tensor-dependent energy E_g^{ε} [69–71]. Here, E_g^0 denotes the bulk value of the band-gap energy of *w*-ZnO ($E_g^0 = 3.37$ eV) [1], and δE_g is its tuning due to the strain. We utilize an expression similar to the one introduced by Wagner *et al.*, who present two different versions for *w*-ZnO, parametrized for either the strain or stress fields, that can be used interchangeably [39,72]. The priming of the coordinate axes of the strain-tensor components in Eq. (4) indicates that the band gaps are computed in the coordinate system local to each of the ZnO material blocks, as described in Sec. II A. Averaged values of E_g^{ε} and δE_g can be computed by averaging their position-dependent counterparts over the volume of the wire for monolithic wires, or over the volume of the ZnO shell for core-shell structures.

Parameters D_1 and D_2 are the associated deformation potentials that were obtained from *ab initio* calculations of Wagner *et al.* [72] and Yan *et al.* [73]. In both of these investigations, hybrid functionals (of the Heyd-Scuseria-Ernzerhof type) are used in combination with exact-exchange-based quasiparticle energy calculations in the G_0W_0 approach specifically to avoid the limitations of generic density-functional-theory techniques in evaluating the electronic properties of *w*-ZnO. Deformation-potential values $D_1 = -5.77$ eV and $D_2 = -2.87$ eV, extracted

TABLE II. Isotropic elastic stiffness-tensor components for smaller ZnO nanowire diameters, along with their corresponding Young's moduli Y, in units of GPa. These values reflect the effect of wire stiffening, as described in Sec. II C. For the 760-nm-diameter nanowire, the averaged bulk values of elastic stiffness-tensor components are used, as presented in the last line of Table I.

Diameter (nm)	C_{11}	C_{12}	C_{44}	Y
260	214.5	96.5	59.0	155.0
100	236.0	106.0	65.0	170.0

from the study by Wagner *et al.* [72], provide accurate band-gap values for larger nanowires with $d \geq 200$ nm. However, for smaller nanowires, a set of deformation potentials reported by Yan *et al.* [73], with values $D_1 = -3.92$ eV and $D_2 = -1.75$ eV, appears to be more accurate than that of Wagner *et al.*, when both sets are compared with the experimental results of Wei *et al.* [35]. The change in the deformation potentials parallels the similar shift in the elastic parameters due to the size-dependent stiffening of the wires.

Turning to the limitations of parametrizations [72,73] associated with Eq. (4), we point out that both of them take into account only certain (symmetry-preserving) kinds of distortions of the *w*-ZnO structure, such as uniaxial distortions along the hexagonal axis and biaxial distortions in the perpendicular plane. More-arbitrary distortions, e.g., those involving shearing, are not included in this expression and thus are not considered in the following analysis. We also note that the deformation-potential parametrizations utilized here do not account for any defect formation in *w*-ZnO that could occur at high strain, potentially having a significant influence on the electronic properties of the nanowires.

III. RESULTS AND DISCUSSION

A. Monolithic ZnO nanowires

The results of our calculations of the volume-averaged values of the axial stress σ_{zz} and band-gap change δE_g in monolithic nanowires subjected to varying degrees of uniaxial tensile strain are shown in Figs. 2(a) and 2(b), respectively. The averaged σ_{xx} and σ_{yy} stress-tensor components are negligibly small in all monolithic nanowires, as, under the applied elastic boundary conditions, their shapes are free to relax into a stress-free equilibrium state in the ***x*-*y*** plane. Experimental data from the investigation of Wei *et al.* [35] is included for comparison in both panels. Both cylindrical and hexagonal nanowire shapes are evaluated; however, it is uncovered that the resulting band-gap changes at a fixed applied tension are nearly identical in both geometries. The computed stress-vs-strain curves display excellent agreement with the experimental results for all three of the considered nanowire diameters. A good agreement with the experimental data is also obtained for the linear δE_g dependence on applied strain for what Wei *et al.* identify as a high-strain regime [35]. The nonlinear low-strain regime that is more prevalent in smaller nanowires is not well represented in our simple model.

The kink in the δE_g dependence on strain could be attributed to a competition between "near-surface" and "near-core" distortions in the nanowires [74], which becomes more prominent as the wire diameter decreases [63]. For example, Yao *et al.* model a monolithic nanowire as a combination of a core region characterized by the bulk ZnO elastic modulus and an enveloping surface region of a finite thickness with a significantly higher elastic modulus [74]. The elastic modulus of the wire then varies with its radius as a result of the surface being significantly stiffer than the core and the wire behavior is dominated by that of the stiffer surface region at a smaller *d*. The influence of the surface-to-volume ratio on the band gap of unstrained ZnO nanowires has been investigated by Chen *et al.* [75], and this work may offer an explanation for the existence of the low-strain regime observed in the experiments of Wei

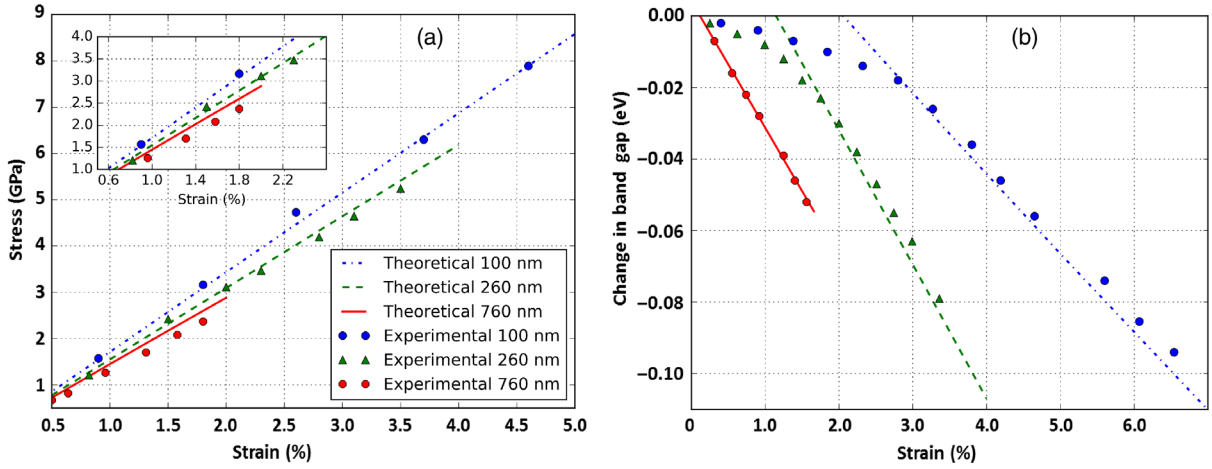

FIG. 2. (a) Stress-vs-strain dependencies for monolithic ZnO nanowires of three different diameters. The experimental data of Wei *et al.* [35] are represented by symbols, and computational results are plotted as solid lines. The Young's modulus *Y* for each nanowire can be determined as the line slope, with specific values given in Table II. (b) Band-gap change δE_g as a function of applied strain for the same nanowires, with the same conventions adopted for presenting the experimental [35] and computational data. Good agreement between the two is achieved in the high-strain regime. The crossover from low to high strain occurs at a strain of approximately 3% for the 100-nm wire and about 1.7% for the 260-nm wire. For the 760-nm wire, only the high-strain regime appears to be pronounced.

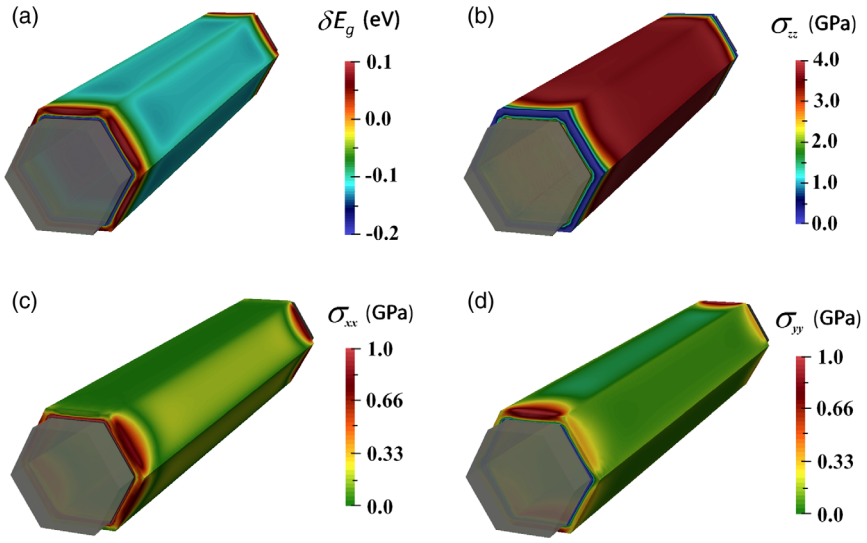

FIG. 3. Spatial distributions of (a) band-gap change δE_g and stress-tensor components (b) σ_{zz}, (c) σ_{xx}, and (d) σ_{yy} throughout the shell region of a hexagonal Zn-ZnO core-shell nanowire with a 300-nm core, 15-nm thick shell and 50-nm core protrusion under 2% tensile strain. Note good axial stress transfer into the shell (b), which results in a large modulation of the band gap within it [approximately −0.12 eV; see (a)]. Note also the complementary symmetrical patterns of the (c) σ_{xx} and (d) σ_{yy} distributions.

et al. [35]. In this context, the critical strain separating the low and high regimes is the one at which the band-gap modulation changes from being surface dominated to being core dominated.

At present, our model of the ZnO nanowire elasticity does not include position-dependent stiffness parameters and therefore it can only reproduce the band-gap modulation in the linear high-strain regime where the wire behavior is dominated by its "bulk" elastic properties. However, the radial variation of the elastic stiffnesses may be incorporated into the model in the next development stage.

B. Zn-ZnO core-shell nanowires

As shown in Fig. 2(b), the highest down-shift of the band gap, which is approximately −0.1 eV, occurs in the 100-nm nanowire at a rather high tensile strain of about 7%. Band-gap shifts in bigger nanowires are not as large, partially because such tensile-strain values cannot be achieved in these structures without breaking them. For example, Wei *et al.* [35] report critical stress of 12.2 GPa at 7.3% tension in the 100-nm nanowire, while, in the 760-nm wire, these values are reduced to 2.4 GPa at 1.7%.

Aiming to overcome this problem and generate even larger band-gap down-shifts, we evaluate a variety of Zn-ZnO core-shell wire geometries, with typical examples presented in Figs. 1(c)–1(e). Our general approach is to utilize the greater plasticity of the metallic core to transfer strain to the thin shell, as well as to optimize the thickness and crystallographic orientation of the shell to obtain the highest possible δE_g. Both cylindrical shapes with a monolithic shell and hexagonal shapes with a composite shell consisting of six individual plates are investigated. In almost all of the cases, the ZnO shell does not cover the core completely—with the latter protruding out by the prescribed distance on both sides of the structure—and had to adjust its shape to satisfy the mechanical equilibrium under the tensile strain applied to the core. Owing to the absence of literature data on the effects of stiffening at such a small scale (the thickness of the shell does not exceed 50 nm for any of the simulations), anisotropic bulk values for the elastic stiffness-tensor components provided in Table I are used to represent the elastic properties of the shell elements.

The results of a typical calculation for equilibrium distributions of the three normal components of the stress tensor, σ_{xx}, σ_{yy}, and σ_{zz}, as well as the band-gap down-shift value δE_g distributions for a strained hexagonal Zn-ZnO core-shell nanowire with a 300-nm core and 15-nm thick shell under 2% tensile strain are displayed in Fig. 3. We observe a good transfer of the axial strain applied to the core into the shell, which results in a large modification of the band gap. Here, an average down-shift of −0.12 eV—larger than the one measured experimentally in the monolithic wires [35]—is projected for the tension of 2%, which, in turn, is substantially lower than the experimental strains of 7% needed to achieve the reported band-gap tuning of −0.1 eV.

A comparison of averaged values of stress-tensor components σ_{zz}, σ_{xx}, and σ_{yy}, and the band-gap change δE_g computed for cylindrical and hexagonal versions of the model with the same shell thickness and other parameters are displayed in Table III. Here, unlike in the situation involving the monolithic wires, we observe that the shape

TABLE III. Average stresses and band-gap shifts in the nanowire with a 300-nm core, 15-nm thick shell and 50-nm core protrusion under 2% tensile strain for both hexagonal and cylindrical core-shell configurations.

Geometry	σ_{zz} (GPa)	σ_{yy} (GPa)	σ_{xx} (GPa)	δE_g (eV)
Hexagonal	3.85	0.09	0.19	−0.12
Cylindrical	2.88	0.10	0.08	−0.09

of the system does influence the value of δE_g significantly. Although the generated average stresses are the same in both structures, the hexagonal-plate shell geometry produces a relatively tight symmetrical grouping of σ_{ij} values compared to a wide scatter of these values in the cylindrical geometry, which leads to fewer cancellations among the different terms during the space averaging of Eq. (4). Furthermore, the σ_{xx} and σ_{yy} stress-tensor components in the core-shell systems are relatively large (roughly a few percent of σ_{zz}) compared to their values in the monolithic wires, and they therefore make a significant contribution to the band-gap drop. This increase originates from considerable interfacial stresses developed at the core-shell boundaries. Inspired by these results, we conduct a series of optimizations of the core-shell system geometrical parameters. The first stage included evaluation of the influence of the length of the core protrusion on the average value of δE_g. For example, a typical dependence of δE_g on core protrusion presented in Fig. 4(a) is obtained for a hexagonal core-shell nanowire with a core size of 200 nm and a 20-nm-thick shell. The initial length of the wire is set to 400 nm with zero protrusion, i.e., with the core and the shell being the same length. On each consecutive step, the length of the core is extended by 10 nm on each side of the wire until the total length of the core reaches 500 nm, while the length of the shell is kept constant. An axial tension of 6% is applied to the core wire in all of the simulations and the average δE_g across the volume of the shell is calculated.

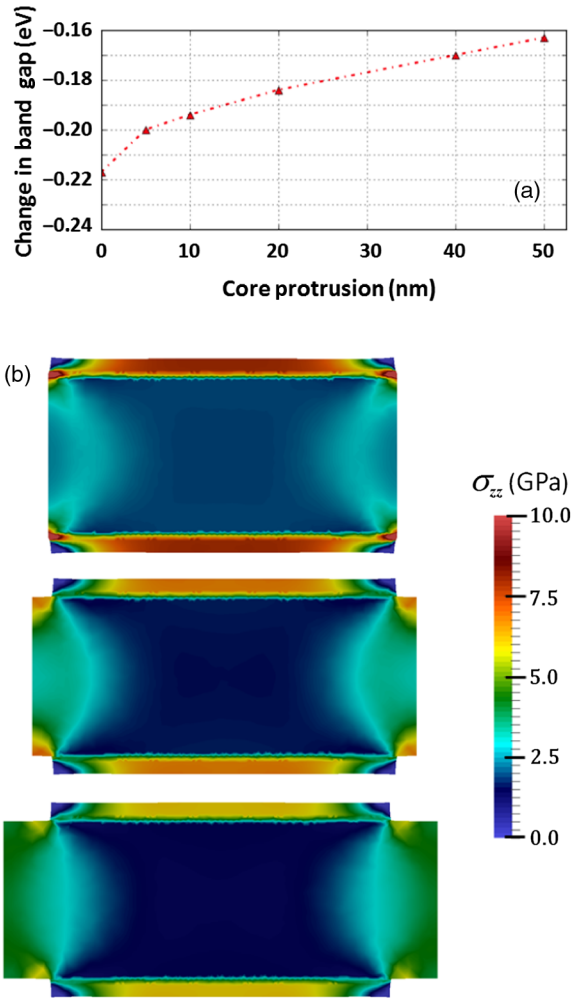

FIG. 4. (a) Dependence of the band-gap shift δE_g on the protrusion of the core beyond the shell. This hexagonal nanowire model utilizes a 400-nm-long and 20-nm-thick shell, and a 200-nm-thick core whose length changes from 400 to 500 nm, protruding up to 50 nm past the length of the shell on either side of the wire. (b) σ_{zz} stress-field distributions in nanowires with (from top to bottom) 0-, 20- and 50-nm core protrusions presented as lengthwise cuts through the structure.

The results of Fig. 4(a) show that δE_g varies sensitively with changing protrusion length for small protrusion values and then saturates for somewhat longer protrusions. This behavior is directly connected with the degree of the applied strain relaxation within the protruding area of the core, i.e., before this strain is transferred into the shell. For shorter protrusions, there is less strain relaxation in the core and the stress fields delivered into the shell are higher, in turn producing larger variation of δE_g. In Fig. 4(b), we present distributions of the σ_{zz} stresses in the nanowires with core protrusions of 0, 20, and 50 nm that have average tensile stresses of 8.5, 7, and 6 GPa, respectively, within the shell region. Note that the corresponding stress values within the core are close to 1.5–2 GPa in all of these structures.

On the next stage of geometry optimization of the core-shell structures, we investigate the influence of changing the applied strain and shell thickness on δE_g. Tensions of up to 7% are considered for shell thicknesses of up to 50 nm. We should point out that, although the values of the induced strains are relatively high, they result in internal shell stresses of less than 8 GPa, which is below the critical value reported by Wei *et al.* [35] for the failure of a 100-nm monolithic ZnO nanowire. These stresses are also well below the value that could induce a transition of *w*-ZnO into a rocksalt structure [76], which is currently not parametrized within our modeling approach.

The results of our simulations for a hexagonal core-shell nanowire with the core size of 200 nm and no core protrusion are shown in Fig. 5. We observe an increase in δE_g with growing applied tension and diminishing thickness of the shell. The latter effect is connected with gradual relaxation of stress fields induced at the core-shell interface within the shell volume as the shell becomes thicker. Nevertheless, for shell thicknesses below 20 nm combined with tensions of 6% to 7% (that still fall within the range of strains that were generated experimentally in monolithic nanowires [35]), a significant band-gap decrease of 0.20 to 0.25 eV is obtained, as shown in the upper-left corner of Fig. 5, which constitutes more than a 100% improvement over the results of Wei *et al.* [35]. The

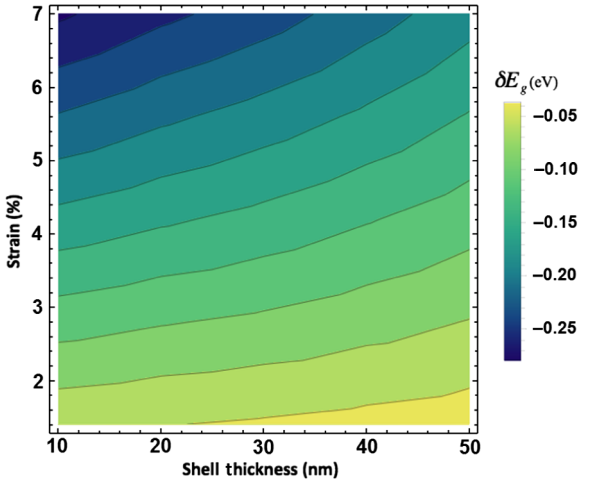

FIG. 5. Averaged band-gap change δE_g in a hexagonal Zn-ZnO nanowire with a 200-nm core, a shell thickness varying from 10 to 50 nm and no core protrusion, subjected to tensile strains ranging from 0% to 7%. Stronger band-gap modulation is achieved in thinner shells.

maximum δE_g obtained for this system is −0.3 eV at 7% tension and a shell thickness of 10 nm.

Finally, on the last stage of geometry optimization for the hexagonal core-shell structures, we investigate the sensitivity of δE_g towards the change of tensorial axis orientation within the shell plates. As already mentioned in Sec. II A, the orientation of the elastic-tensor axes in each shell plate is adjustable by a sequence of $\mathbf{Z}_1(\theta)\mathbf{X}_2(\phi)\mathbf{Z}_3(\Psi)$ Euler rotations. Starting from the initial local coordinate system orientation of $\mathbf{Z}_1(0)\mathbf{X}_2(0)\mathbf{Z}_3(0)$ in each plate, i.e., $z' \| z$ and x' perpendicular to the plate surface, we conduct a series of $\mathbf{Z}_1(\theta)$ rotations in three degree increments, while also sweeping through $\mathbf{X}_2(\phi)$ rotation in three degree increments for each value of θ.

The results of our simulations for a nanowire with a 200-nm core and 20-nm thick shell subjected to an applied tensile strain of 3% are presented in Fig. 6(a). Figure 6(b) contains sketches for the initial $\mathbf{Z}_1(0)\mathbf{X}_2(0)\mathbf{Z}_3(0)$ orientation of the primed axes, as well as their $\mathbf{Z}_1(\theta)$ and $\mathbf{X}_2(\phi)$ rotations. We observe no variation in the value of δE_g for the $\mathbf{Z}_1(\theta)$ rotations, i.e., for those that only change the mutual orientation of the x' and y' axes while leaving the z' axis parallel to the z axis of the nanowire. On the other hand, the influence of $\mathbf{X}_2(\phi)$ rotations that change the orientation of the z' axis relative to the nanowire axis is more pronounced and results in a drop in δE_g as the angle between the axes increases. In the limiting case of $\phi = 90°$ that is equivalent to the z' axis being perpendicular to the axis of the nanowire a zero band-gap shift is detected.

This behavior stems from the anisotropic relation between the elastic distortions and electronic properties of w-ZnO, as exemplified by Eq. (4). Owing to the strong dependence of the w-ZnO band gap upon uniaxial distortions along the hexagonal axis and its much weaker dependence on biaxial distortions in the perpendicular crystallographic plane, the largest δE_g modulation is observed when this axis is aligned with the nanowire axis, while the smallest modulation occurs when these axes are perpendicular to each other.

Finally, we point out that the results of our analysis should be applicable to core-shell nanowires of other—including larger—sizes, as opposed to those considered here, as long as their elastic properties are independent of the actual dimensions and their core-shell thickness ratios are comparable. The situation is less clear for *smaller* nanowires since the stress and shape dependence of their band gaps, including any possible size-dependent transitions, has not yet been exhaustively studied.

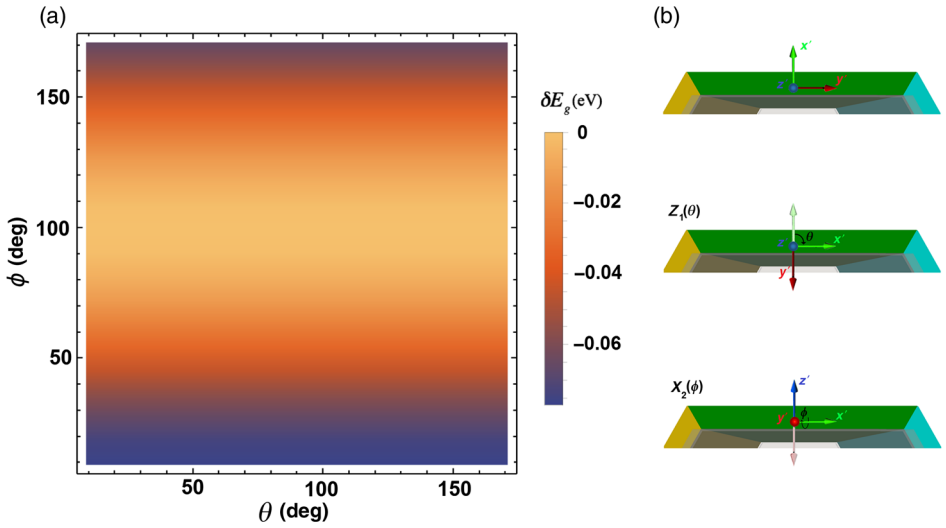

FIG. 6. (a) The influence of the $\mathbf{X}_2(\phi)$ and $\mathbf{Z}_1(\theta)$ Euler rotations of the elastic stiffness-tensor axes within the ZnO shell plate on the value of the band-gap shift δE_g. The hexagonal nanowire model used here has a 200-nm Zn core, a 20-nm-thick ZnO shell, and a core protrusion of 50 nm and is subjected to an applied tensile strain of 3%. There is no variation in the band-gap value for the $\mathbf{Z}_1(\theta)$ rotations, i.e., those that preserve the alignment of the z' axis with the z axis of the nanowire. The $\mathbf{X}_2(\phi)$ rotations that break the alignment between the z' and z axes produce a decrease in δE_g, with $\mathbf{X}_2(90°)$ resulting in a zero band-gap shift. (b) Sketches of the Euler rotations of the stiffness-tensor axes.

IV. CONCLUSIONS

In this paper, we investigate strain-induced band-gap tuning in monolithic ZnO nanowires utilizing a FEM-based approach parametrized from *ab initio* simulations. Typical nanowire dimensions are 400–500 nm in length and 100 nm to 1 μm across. Both cylindrical and hexagonal wire shapes are evaluated. For monolithic nanowires, good agreement between our calculations and the available experimental results is obtained for their stress-vs-strain and band-gap modulation dependencies under applied axial tension, with the maximum average band-gap shift of −0.1 eV found in the 100-nm wire subjected to a 7% tensile strain. It is also determined that variations of the wire shape do not change their elastic response and band-gap tuning appreciably.

The same modeling approach is then employed to predictively evaluate the strain-induced band-gap modulation in Zn-ZnO core-shell nanowire configurations, as well as to optimize their geometry in order to enhance this effect. The influences of the wire shape (hexagonal or cylindrical), core protrusion beyond the shell, shell thickness, and elastic-tensor axis orientations within the shell are taken into account. We find that, due to their high symmetry, hexagonal shapes of the core-shell nanowires produce stronger band-gap tunings. Furthermore, smaller core protrusions combined with thinner shells and an alignment of hexagonal crystallographic axes of metallic Zn and *w*-ZnO along the axis of the nanowire also result in stronger band-gap modulation for the same value of applied tensile strain. For example, we observe band-gap shifts of up to −0.3 eV (i.e., approx. 10% of the *w*-ZnO band-gap value) in a nanowire with a 200-nm core cross section and 10-nm-thick shell under 7% axial tension. While, *by itself*, such a band-gap shift is still insufficient for mainstream photovoltaic applications, we presume that combining it with other chemical and physical mechanisms for electronic properties tuning, including composition and defect engineering, may produce even greater band-gap down-shifts that will be useful for efficient photovoltaic energy conversion.

We believe that computational results presented here will improve our understanding of complex size- and shape-dependent properties of 1D semiconductors at nano- and mesoscale, and they will serve as a guide for future experimental efforts aimed at the synthesis and characterization of these interesting nanostructures. Although the Zn-ZnO core-shell nanowires studied here are, as of now, hypothetical, a number of similar heterostructures involving Zn-ZnO interfaces have already been made [42,44,77,78]. Therefore, we hope that such nanowires can be synthesized by employing analogous growth techniques.

[1] Sven Barth, Francisco Hernandez-Ramirez, Justin D. Holmes, and Albert Romano-Rodriguez, Synthesis and applications of one-dimensional semiconductors, Prog. Mater. Sci. **55**, 563 (2010).

[2] Zhong Lin Wang, Functional oxide nanobelts: Materials, properties and potential applications in nanosystems and biotechnology, Annu. Rev. Phys. Chem. **55**, 159 (2004).

[3] Zhong Lin Wang and Jinhui Song, Piezoelectric nanogenerators based on zinc oxide nanowire arrays, Science **312**, 242 (2006).

[4] Zhong Lin Wang, ZnO nanowire and nanobelt platform for nanotechnology, Mater. Sci. Eng. R **64**, 33 (2009).

[5] Sanghyun Ju, Antonio Facchetti, Yi Xuan, Jun Liu, Fumiaki Ishikawa, Peide Ye, Chongwu Zhou, Tobin J. Marks, and David B. Janes, Fabrication of fully transparent nanowire transistors for transparent and flexible electronics, Nat. Nanotechnol. **2**, 378 (2007).

[6] Mohammed Riaz, Jinhui Song, Omer Nur, Zhong Lin Wang, and Magnus Willander, Study of the piezoelectric power generation of ZnO nanowire arrays grown by different methods, Adv. Funct. Mater. **21**, 628 (2011).

[7] Zheng Wei Pan, Zu Rong Dai, and Zhong Lin Wang, Nanobelts of semiconducting oxides, Science **291**, 1947 (2001).

[8] A. Asthana, K. Momeni, A. Prasad, Y. K. Yap, and R. S. Yassar, In situ observation of size-scale effects on the mechanical properties of ZnO nanowires, Nanotechnology **22**, 265712 (2011).

[9] Innocent Udom, Manoj K. Ram, Elias K. Stefanakos, Aloysius F. Hepp, and D. Yogi Goswami, One dimensional-ZnO nanostructures: Synthesis, properties and environmental applications, Mater. Sci. Semicond. Process. **16**, 2070 (2013).

[10] Ü Özgür, Ya I. Alivov, Chunli Liu, A. Teke, M. A. Reshchikov, S Doğan, V. C. S. J. Avrutin, S.-J. Cho, and H. Morkoc, A comprehensive review of ZnO materials and devices, J. Appl. Phys. **98**, 041301 (2005).

[11] Neil P. Dasgupta, Jianwei Sun, Chong Liu, Sarah Brittman, Sean C. Andrews, Jongwoo Lim, Hanwei Gao, Ruoxue Yan, and Peidong Yang, 25th anniversary article: Semiconductor nanowires—Synthesis, characterization, and applications, Adv. Mater. **26**, 2137 (2014).

[12] Zhong Lin Wang, Zinc oxide nanostructures: Growth, properties and applications, J. Phys. Condens. Matter **16**, R829 (2004).

[13] Pai-Chun Chang, Zhiyong Fan, Chung-Jen Chien, Daniel Stichtenoth, Carsten Ronning, and Jia Grace Lu, High-performance ZnO nanowire field effect transistors, Appl. Phys. Lett. **89**, 133113 (2006).

[14] Josh Goldberger, Donald J. Sirbuly, Matt Law, and Peidong Yang, ZnO nanowire transistors, J. Phys. Chem. B **109**, 9 (2005).

[15] Minbaek Lee, Chih-Yen Chen, Sihong Wang, Seung Nam Cha, Yong Jun Park, Jong Min Kim, Li-Jen Chou, and Zhong Lin Wang, A hybrid piezoelectric structure for wearable nanogenerators, Adv. Mater. **24**, 1759 (2012).

[16] Peidong Yang, Ruoxue Yan, and Melissa Fardy, Semiconductor nanowire: What's next?, Nano Lett. **10**, 1529 (2010).

[17] Joshua Schrier, Denis O. Demchenko, and A. Paul Alivisatos, Optical properties of ZnO/ZnS and ZnO/ZnTe heterostructures for photovoltaic applications, Nano Lett. **7**, 2377 (2007).

[18] Benjamin Weintraub, Zhengzhi Zhou, Yinhua Li, and Yulin Deng, Solution synthesis of one-dimensional ZnO nanomaterials and their applications, Nanoscale **2**, 1573 (2010).
[19] P. Sudhagar, R. Saravana Kumar, June Hyuk Jung, Woohyung Cho, R. Sathyamoorthy, Jongok Won, and Yong Soo Kang, Facile synthesis of highly branched jacks-like ZnO nanorods and their applications in dye-sensitized solar cells, Mater. Res. Bull. **46**, 1473 (2011).
[20] Miao Yu, Yun-Ze Long, Bin Sun, and Zhiyong Fan, Recent advances in solar cells based on one-dimensional nanostructure arrays, Nanoscale **4**, 2783 (2012).
[21] Liwen Sang, Meiyong Liao, and Masatomo Sumiya, A comprehensive review of semiconductor ultraviolet photodetectors: From thin film to one-dimensional nanostructures, Sensors **13**, 10482 (2013).
[22] Thushara J. Athauda, Parameswar Hari, and Ruya R. Ozer, Tuning physical and optical properties of ZnO nanowire arrays grown on cotton fibers, ACS Appl. Mater. Interfaces **5**, 6237 (2013).
[23] Mei-Lin Zhang, Feng Jin, Mei-Ling Zheng, Jie Liu, Zhen-Sheng Zhao, and Xuan-Ming Duan, High efficiency solar cell based on ZnO nanowire array prepared by different growth methods, RSC Adv. **4**, 10462 (2014).
[24] Xu Xiao, Longyan Yuan, Junwen Zhong, Tianpeng Ding, Yu Liu, Zhixiang Cai, Yaoguang Rong, Hongwei Han, Jun Zhou, and Zhong Lin Wang, High-strain sensors based on ZnO nanowire/polystyrene hybridized flexible films, Adv. Mater. **23**, 5440 (2011).
[25] Qing Wan, Q. H. Li, Y. J. Chen, Ta-Hung Wang, X. L. He, J. P. Li, and C. L. Lin, Fabrication and ethanol sensing characteristics of ZnO nanowire gas sensors, Appl. Phys. Lett. **84**, 3654 (2004).
[26] Punniamoorthy Ravirajan, Ana M. Peiró, Mohammad K. Nazeeruddin, Michael Graetzel, Donal D. C. Bradley, James R. Durrant, and Jenny Nelson, Hybrid polymer/zinc oxide photovoltaic devices with vertically oriented ZnO nanorods and an amphiphilic molecular interface layer, J. Phys. Chem. B **110**, 7635 (2006).
[27] Neil P. Dasgupta and Peidong Yang, Semiconductor nanowires for photovoltaic and photoelectrochemical energy conversion, Front. Phys. **9**, 289 (2014).
[28] Safa Shoaee, Joe Briscoe, James R. Durrant, and Steve Dunn, Acoustic enhancement of polymer/ZnO nanorod photovoltaic device performance, Adv. Mater. **26**, 263 (2014).
[29] Long Yang, Qing-lan Ma, Yungao Cai, and Yuan Ming Huang, Enhanced photovoltaic performance of dye sensitized solar cells using one dimensional ZnO nanorod decorated porous TiO_2 film electrode, Appl. Surf. Sci. **292**, 297 (2014).
[30] Jonathan D. Major, Ramon Tena-Zaera, Eneko Azaceta, L. Bowen, and K. Durose, Development of ZnO nanowire based CDTE thin film solar cells, Sol. Energy Mater. Sol. Cells **160**, 107 (2017).
[31] Yangyang Zhang, Manoj K. Ram, Elias K. Stefanakos, and D. Yogi Goswami, Synthesis, characterization and applications of ZnO nanowires, J. Nanomater. **2012**, 624520 (2012).
[32] Son Hoang and Pu-Xian Gao, Nanowire array structures for photocatalytic energy conversion and utilization: A review of design concepts, assembly and integration, and function enabling, Adv. Energy Mater. **6**, 1600683 (2016).
[33] Y. W. Chen, Y. C. Liu, S. X. Lu, C. S. Xu, C. L. Shao, C. Wang, J. Y. Zhang, Y. M. Lu, D. Z. Shen, and X. W. Fan, Optical properties of ZnO and ZnO:In nanorods assembled by sol-gel method, J. Chem. Phys. **123**, 134701 (2005).
[34] Guozhen Shen, Jung Hee Cho, Jin Kyoung Yoo, Gyu-Chul Yi, and Cheol Jin Lee, Synthesis and optical properties of *S*-doped ZnO nanostructures: Nanonails and nanowires, J. Phys. Chem. B **109**, 5491 (2005).
[35] Bin Wei, Kun Zheng, Yuan Ji, Yuefei Zhang, Ze Zhang, and Xiaodong Han, Size-dependent bandgap modulation of ZnO nanowires by tensile strain, Nano Lett. **12**, 4595 (2012).
[36] Rui-wen Shao, Kun Zheng, Bin Wei, Yue-fei Zhang, Yu-jie Li, Xiao-dong Han, Ze Zhang, and Jin Zou, Bandgap engineering and manipulating electronic and optical properties of ZnO nanowires by uniaxial strain, Nanoscale **6**, 4936 (2014).
[37] Waheed A. Adeagbo, Stefan Thomas, Sanjeev K. Nayak, Arthur Ernst, and Wolfram Hergert, First-principles study of uniaxial strained and bent ZnO wires, Phys. Rev. B **89**, 195135 (2014).
[38] Kentaro Watanabe, Takahiro Nagata, Yutaka Wakayama, Takashi Sekiguchi, Róbert Erdélyi, and János Volk, Bandgap deformation potential and elasticity limit of semiconductor free-standing nanorods characterized in situ by scanning electron microscope–cathodoluminescence nanospectroscopy, ACS Nano **9**, 2989 (2015).
[39] John Mangeri, Olle Heinonen, Dmitry Karpeyev, and Serge Nakhmanson, Influence of Elastic and Surface Strains on the Optical Properties of Semiconducting Core-Shell Nanoparticles, Phys. Rev. Applied **4**, 014001 (2015).
[40] TRELIS is a nongovernment version of the CUBIT software package developed by Sandia National Laboratories and is available at www.csimsoft.com/trelis.
[41] Pu Xian Gao and Zhong L. Wang, Nanoarchitectures of semiconducting and piezoelectric zinc oxide, J. Appl. Phys. **97**, 044304 (2005).
[42] Pu Xian Gao, Chang Shi Lao, Yong Ding, and Zhong Lin Wang, Metal/semiconductor core/shell nanodisks and nanotubes, Adv. Funct. Mater. **16**, 53 (2006).
[43] Xiang Yang Kong, Yong Ding, and Zhong Lin Wang, Metal-semiconductor Zn-ZnO core-shell nanobelts and nanotubes, J. Phys. Chem. B **108**, 570 (2004).
[44] J. Q. Hu, Q. Li, X. M. Meng, C. S. Lee, and S. T. Lee, Thermal reduction route to the fabrication of coaxial Zn/ZnO nanocables and ZnO nanotubes, Chem. Mater. **15**, 305 (2003).
[45] J. Noborisaka, J. Motohisa, and T. Fukui, Catalyst-free growth of GaAs nanowires by selective-area metalorganic vapor-phase epitaxy, Appl. Phys. Lett. **86**, 213102 (2005).
[46] Stephen D. Hersee, Xinyu Sun, and Xin Wang, The controlled growth of GaN nanowires, Nano Lett. **6**, 1808 (2006).
[47] K. A. Nertness, A. Roshko, N. A. Sanford, J. M. Barker, and A. V. Davydov, Spontaneously grown GaN and AlGaN nanowires, J. Cryst. Growth **287**, 522 (2006).
[48] S. Venkatesan, M. H. Madsen, H. Schmid, P. Krogstrup, E. Johnson, and C. Scheu, Direct observation of interface and nanoscale compositional modulation in ternary III-As heterostructure nanowires, Appl. Phys. Lett. **103**, 063106 (2013).

[49] Haibo Zeng, Weiping Cai, Jinlian Hu, Guotao Duan, Peisheng Liu, and Yue Li, Violet photoluminescence from shell layer of Zn/ZnO core-shell nanoparticles induced by laser ablation, Appl. Phys. Lett. **88**, 171910 (2006).
[50] Haibo Zeng, Weiping Cai, Bingqiang Cao, Jinlian Hu, Yue Li, and Peisheng Liu, Surface optical phonon Raman scattering in Zn/ZnO core-shell structured nanoparticles, Appl. Phys. Lett. **88**, 181905 (2006).
[51] H. Zeng, Z. Li, W. Cai, B. Cao, P. Liu, and S. Yang, Microstructure control of Zn/ZnO core/shell nanoparticles and their temperature-dependent blue emissions, J. Phys. Chem. B **111**, 14311 (2007).
[52] O. Lupan, L. Chow, G. Chai, and H. Heinrich, Fabrication and characterization of Zn-ZnO core-shell microspheres from nanorods, Chem. Phys. Lett. **465**, 249 (2008).
[53] Dai-ming Tang, Gang Liu, Feng Li, Jun Tan, Chang Liu, Gao Qing Lu, and Hui-ming Cheng, Synthesis and photoelectrochemical property of urchin-like Zn/ZnO core-shell structures, J. Phys. Chem. C **113**, 11035 (2009).
[54] John Frederick Nye, *Physical Properties of Crystals* (Oxford University Press, New York, 1985).
[55] H. M. Ledbetter, Elastic properties of zinc: A compilation and a review, J. Phys. Chem. Ref. Data **6**, 1181 (1977).
[56] T. B. Bateman, Elastic moduli of single-crystal zinc oxide, J. Appl. Phys. **33**, 3309 (1962).
[57] Morton E. Gurtin and A. Ian Murdoch, A continuum theory of elastic material surfaces, Arch. Ration. Mech. Anal. **57**, 291 (1975).
[58] J. Yvonnet, A. Mitrushchenkov, G. Chambaud, and Q.-C. He, Finite element model of ionic nanowires with size-dependent mechanical properties determined by ab initio calculations, Comput. Methods Appl. Mech. Eng. **200**, 614 (2011).
[59] J. Yvonnet, A. Mitrushchenkov, G. Chambaud, Q.-C. He, and S.-T. Gu, Characterization of surface and nonlinear elasticity in wurtzite ZnO nanowires, J. Appl. Phys. **111**, 124305 (2012).
[60] FERRET is an open-source module for the MOOSE software package and is available at https://bitbucket.org/mesoscience/ferret.
[61] The open-source MOOSE project was developed by Idaho National Laboratory and is available at http://mooseframework.org/.
[62] Derek Gaston, Chris Newman, Glen Hansen, Damien Lebrun-Grandie, and Damien Lebrun-Grandié, MOOSE: A parallel computational framework for coupled systems of nonlinear equations, Nucl. Eng. Des. **239**, 1768 (2009).
[63] C. Q. Chen, Y. Shi, Y. S. Zhang, J. Zhu, and Y. J. Yan, Size Dependence of Young's Modulus in ZnO Nanowires, Phys. Rev. Lett. **96**, 075505 (2006).
[64] Guofeng Wang and Xiaodong Li, Size dependency of the elastic modulus of ZnO nanowires: Surface stress effect, Appl. Phys. Lett. **91**, 231912 (2007).
[65] Ravi Agrawal, Bei Peng, Eleftherios E. Gdoutos, and Horacio D. Espinosa, Elasticity size effects in ZnO nanowires—A combined experimental-computational approach, Nano Lett. **8**, 3668 (2008).
[66] Mo-Rigen He, Y. Shi, W. Zhou, J. W. Chen, Y. J. Yan, and J Zhu, Diameter dependence of modulus in zinc oxide nanowires and the effect of loading mode: In situ experiments and universal core-shell approach, Appl. Phys. Lett. **95**, 091912 (2009).
[67] Feng Xu, Qingqun Qin, Ashish Mishra, Yi Gu, and Yong Zhu, Mechanical properties of ZnO nanowires under different loading modes, Nano Res. **3**, 271 (2010).
[68] Xiaoguang Wang, Kai Chen, Yongqiang Zhang, Jingchun Wan, Oden L. Warren, Jason Oh, Ju Li, Evan Ma, and Zhiwei Shan, Growth conditions control the elastic and electrical properties of ZnO nanowires, Nano Lett. **15**, 7886 (2015).
[69] A. Gavini and M. Cardona, Modulated piezoreflectance in semiconductors, Phys. Rev. B **1**, 672 (1970).
[70] W. Shan, R. J. Hauenstein, A. J. Fischer, J. J. Song, W. G. Perry, M. D. Bremser, R. F. Davis, and B. Goldenberg, Strain effects on excitonic transitions in GaN: Deformation potentials, Phys. Rev. B **54**, 13460 (1996).
[71] L. C. Lew, Yan Voon, and M. Willatzen, *The* ***k·p*** *Method: Electronic Properties of Semiconductors* (Springer, New York, 2009).
[72] Markus R. Wagner, Gordon Callsen, Juan S. Reparaz, Ronny Kirste, Axel Hoffmann, Anna V. Rodina, André Schleife, Friedhelm Bechstedt, and Matthew R. Phillips, Effects of strain on the valence band structure and exciton-polariton energies in ZnO, Phys. Rev. B **88**, 235210 (2013).
[73] Qimin Yan, Patrick Rinke, Momme Winkelnkemper, Abdallah Qteish, Dieter Bimberg, Matthias Scheffler, and Chris G. Van de Walle, Strain effects and band parameters in MgO, ZnO, and CdO, Appl. Phys. Lett. **101**, 152105 (2012).
[74] Haiyan Yao, Guohong Yun, Narsu Bai, and Jiangang Li, Surface elasticity effect on the size-dependent elastic property of nanowires, J. Appl. Phys. **111**, 083506 (2012).
[75] Chun-Wei Chen, Kuei-Hsien Chen, Ching-Hsing Shen, Abhijit Ganguly, Li-Chyong Chen, Jih-Jen Wu, Hui-I Wen, and Way-Faung Pong, Anomalous blueshift in emission spectra of ZnO nanorods with sizes beyond quantum confinement regime, Appl. Phys. Lett. **88**, 241905 (2006).
[76] J. M. Recio, M. A. Blanco, V. Luaña, Ravindra Pandey, L. Gerward, and J. Staun Olsen, Compressibility of the high-pressure rocksalt phase of ZnO, Phys. Rev. B **58**, 8949 (1998).
[77] Jih Jen Wu, Sai Chang Liu, Chien Ting Wu, Kuei Hsien Chen, and Li Chyong Chen, Heterostructures of ZnO-Zn coaxial nanocables and ZnO nanotubes, Appl. Phys. Lett. **81**, 1312 (2002).
[78] Pu Xian Gao and Zhong Lin Wang, Mesoporous polyhedral cages and shells formed by textured self-assembly of ZnO nanocrystals, J. Am. Chem. Soc. **125**, 11299 (2003).